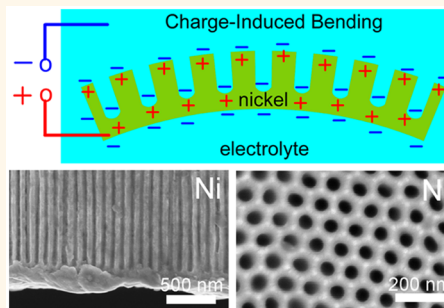# Reversible Electrochemical Actuation of Metallic Nanohoneycombs Induced by Pseudocapacitive Redox Processes

Chuan Cheng* and Alfonso H. W. Ngan

Department of Mechanical Engineering, The University of Hong Kong, Hong Kong, People's Republic of China

ABSTRACT Current metallic-based electrochemical actuators are limited to nanoporous gold/platinum with randomly distributed pores, where the charge-induced reversible strain is mainly due to the nonfaradic charging/discharging processes along the capacitive electrochemical double layer. Here, we report an electrochemical actuating property of nanohoneycomb-structured nickel, with the actuation mechanism mainly due to a pseudocapacitive behavior by means of reversible faradic redox reactions. By using a dual-template synthesis method, a bilayered cantilever, comprising a nanohoneycomb layer backed by a solid layer of the same metal, was fabricated. Reversible bending of the cantilever upon cyclic potential triggering was observed. The strain of the cantilever increases nonlinearly with both potential and charge due to redox reactions. The maximum strain that can be achieved under a certain scan rate complies with a linear relationship with the capacity. Benefiting from the stable Ni(II)/Ni(III) redox couples at the electrode surface, the reversible actuation is very stable in hydroxide solutions.

KEYWORDS: nanohoneycomb nickel · electrochemical actuation · surface-charge-induced strain · reversible redox reactions · electrochemical double layer

Human skeletal muscles are ideal actuators with large strain amplitudes (>40%), fast strain response (>50%/s), high energy efficiency (~40%), and durability (>10^9 life cycles).[1] Materials that can mimic the properties of muscles upon outside electrical/chemical triggering are known as "artificial muscles", which may serve, for instance, as the building blocks of robots.[2−5] Nowadays, piezoceramics, electroactive polymers, and shape memory alloys have already been commercialized as actuation materials for artificial muscle applications.[6,7] However, their use is limited by factors including ultrahigh actuation voltages needed (>1 kV for both piezoceramics and electroactive polymers), small strain amplitudes (~0.1% for piezoceramics), and low energy efficiency (~3% for shape memory alloys).[1,8] In the past decade, increasing attention has been paid to a diverse group of nanoporous materials for electrochemical actuations, including nanoporous noble metals,[9−13] carbon nanotubes,[1,3,14−20] conducting polymers,[1,3] carbon aerogels,[16,21] and graphene films,[22−24] to transform electrical energy into mechanical energy for potential applications as artificial muscles.[25] Due to the low triggering voltages for the electrochemical process in the actuation mechanism, these nanoporous materials require voltages on the order of 1 V to actuate, which is about 3 orders of magnitude lower than that for conventional actuation materials,[6,7] such as piezoceramics, which require high voltages to realize dipole alignment in the bulk, while the actuation strain achievable is comparable to, or even 1 order of magnitude higher than, these conventional actuation materials.

In spite of the above, many challenges still need to be overcome before nanostructured materials can be widely used in practical actuation applications.[1−5,26] Although polymer-based actuation materials have large charge-induced reversible strains (>100%), they suffer from slow response times[21,27] and low stiffness and strengh.[9] Metallic-based nanoporous materials are competitive candidates for electrochemical actuators in terms of their much better stiffness and strength. Furthermore, by decreasing the ligament size in these nanoporous metals, not only can the yield strength and stiffness be enhanced,[28−30]
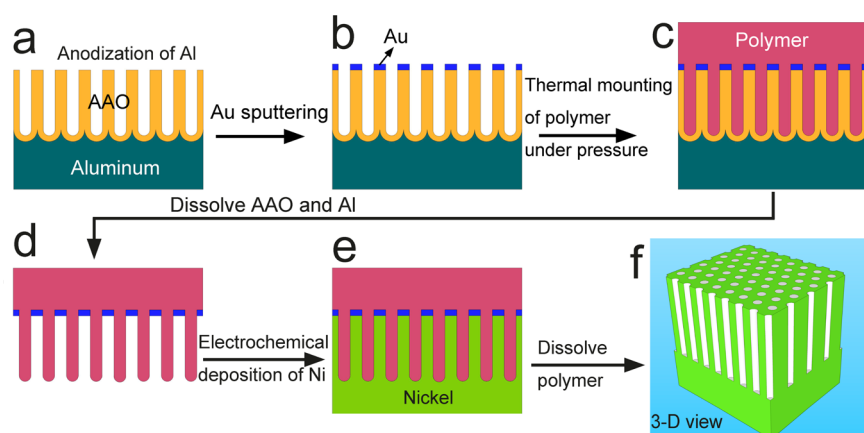
Figure 1. Schematic of the fabrication process of an ordered nanohoneycomb Ni layer backed by a solid Ni layer. (a) AAO template; (b) Au sputtering on the top surface of the AAO template; (c) polymer mounting into the AAO template; (d) inverse polymer template; (e) electrochemical deposition of Ni into the polymer template; (f) 3-D view of the bilayered nanohoney-comb/solid Ni foil.

but the actuation strain can also be increased because the strain is proportional to the surface-area-to-volume ratio.[12]

However, the nanoporous metals that have been studied to date have certain limitations. First, these metallic-based electrochemical actuators are restricted to noble metals, such as Pt,[12] Au,[5,9] and Au−Pt composites,[9] because of their unique properties including the high redox potentials and small accessible ligament size (<10 nm). Other metals,[31−35] such as Ag, Ni, and Cu, which were made by dealloying,[36,37] were found to exhibit relatively larger ligament size and contain frequent cracks, which limit their actuation performance.[38] Second, nanoporous noble metals made by dealloying methods have randomly distributed porous structures, and as a result, the charge-induced stresses between neighboring nanoligaments are not efficiently exploited and may even be partially canceled.[39−41]

Furthermore, in terms of the electrochemical actuation mechanism, the strain in nanoporous noble metals has been demonstrated to be induced by charges.[12] However, charges can be stored at the electrode/electrolyte interface in two ways: one is the nonfaradic charging along the capacitive electrochemical double layer, and the other is the faradic redox reactions, the so-called pseudocapacitive processes.[42] The nonfaradic process is associated with the potential-dependent accumulation of charges by means of electrolyte ion movement, reorientation of solvent dipoles, and ion adsorption/desorption, while the faradic process is associated with electrochemical reactions. This difference in charge storage may result in different mechanisms for charge-induced strain at the electrode surface. For the nonfaradic case, the charge accumulation at the capacitive double-layer can induce electron redistribution among the surface atoms of the electrode, resulting in changing of the bond strength and the equilibrium interatomic distance, and, thus, strain.[12,43−45] This type of charge-induced strain has been found in

nanoporous Pt[12] and Au,[36] in which the strain linearly increases with potential, within a region corresponding to the purely capacitive double layer.[12,36] However, for the faradic case, charges are not accumulated but stored within the reaction products along the electrode surface. The reaction products may have different lattice structures or volumes compared with the substrate materials, and as a result, strain may be induced by lattice mismatch or volume expansion/contraction. To our knowledge, little attention has been paid to this possible mechanism for charge-induced strain, possibly due to the lack of electrochemical actuation materials that exhibit obvious redox reactions upon actuation. This is another significant point of this work.

Here, we demonstrate a cantilever-shaped and nickel-based electrochemical actuator, which consists of a highly ordered nanohoneycomb layer backed with a solid layer. Upon cyclic electric charging, reversible strain is induced within the nanohoneycomb nickel layer, mainly due to the reversible redox reactions. Due to the constraint of the solid nickel layer, reversible and macroscopic bending of the cantilever is observed, and the electrochemical properties are characterized *in situ*. The strain increases with potential and charge in a nonlinear manner, and a very simple linear relationship between electrochemical capacity and strain is observed. The nanohoneycomb structure in nickel is duplicated from self-ordered anodic aluminum oxide (AAO), by a two-template-based method. The present actuating material system studied is significantly different from the previously studied counterparts of nanoporous noble metals, in terms of the nanoporous architecture, synthesis method, and actuation mechanism, and is also low-cost to fabricate.

RESULTS AND DISCUSSION

Fabrication and Microstructure Characterization of Bilayered Nanohoneycomb/Solid Ni. Figure 1 illustrates the fabrication
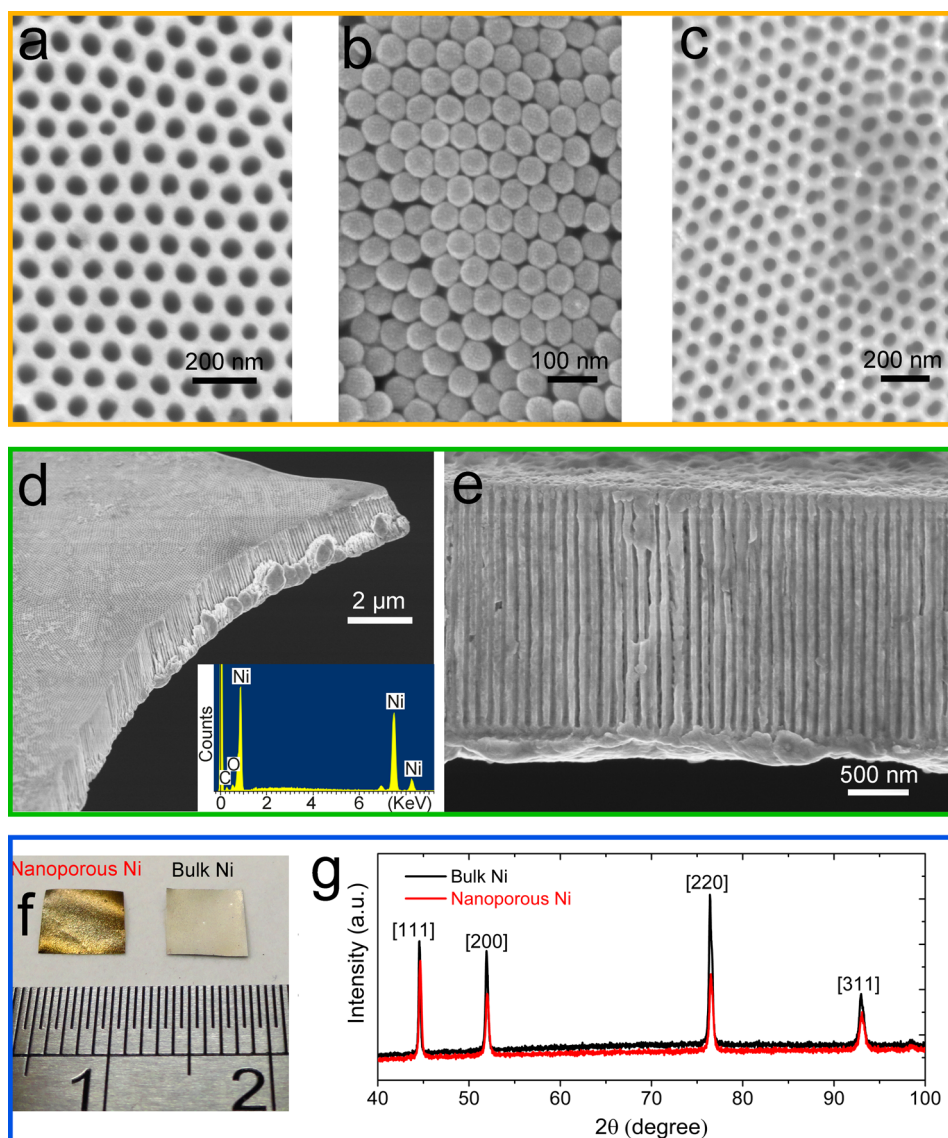
Figure 2. (a) AAO template formed by high-acid-concentration and high-temperature anodization method (40 V, 0.9 M H$_2$C$_2$O$_4$, 20 °C, 1st step 3 h, 2nd step 5 min). (b) Polymer inverse template fabricated from the AAO template. (c) Top view of nanohoneycomb Ni duplicating the structure of the AAO template in (a). (d, e) Cross-sectional views of nanohoneycomb Ni corresponding to (c). (f) Top-view photo for comparison between nanohoneycomb Ni and solid Ni (without the nanohoneycomb structures). (g) X-ray diffraction corresponding to nanohoneycomb Ni and solid Ni shown in (f).

process of the bilayered nanohoneycomb/solid Ni structure (see Methods section). Essentially, such a structure is produced by electrodeposition of Ni on an inverse polymer template (Figure 1d), which is in turn fabricated by molding onto a highly ordered nanohoneycomb AAO template (Figure 1a). The use of the polymer as an inverse template, instead of directly electrodepositing Ni onto the AAO template, enables the resultant Ni structure to adopt a similar nanohoneycomb structure to the original AAO template.

By using a recently developed high-acid-concentration and high-temperature anodization method,[46] AAO templates with a highly ordered nanohoneycomb structure were fabricated by two-step anodization of aluminum, as shown in Figure 2a. The top view of the AAO has a quasi-hexagonal pattern with an average

interpore distance of ~96 nm, which is slightly smaller than that obtained by the conventional mild anodization method (~100 nm),[47] because of the effects of the high oxalic acid concentration used.[46] The new method has the advantage of fast fabrication of AAO within about 3 h, compared to typically 2 days in the mild anodization method, and it yields much better ordering quality of the pore channels than the mild anodization method. Within a voltage range from 30 to 60 V in oxalic acid, the interpore distance is tunable from 74 to 112 nm.[46]

From the AAO template in Figure 2a, an inverse template comprising polymer pillar arrays was fabricated by hot mounting into the channels of the AAO under 15 kN pressure at 180 °C, as shown in Figure 2b. After that the AAO template was selectively dissolved,

and then Ni was electrodeposited into the spacing of the inverse polymer template. After selectively dissolving the inverse template, a nanohoneycomb Ni structure that duplicates the quasi-hexagonal pattern of AAO was obtained, as shown in Figure 2c–e. By controlling the electrodeposition time, a backing layer of solid Ni can be deposited outside nanohoneycomb-structured Ni, and a bilayered nanohoneycomb/solid structure can be obtained. In Figure 2c–e, the electrochemical deposition time was selected to be 20 min, so that a thin layer ($\sim$0.18 μm) of solid Ni was made to just cover up a much thicker ($\sim$2.0 μm) layer of nanohoneycomb Ni. The inset in Figure 2d shows energy-dispersive X-ray spectroscopy results from a cross-section of a nanohoneycomb Ni layer in Figure 2e, which confirm that the fabricated material consists mainly of nickel.

This dual-template-based, nonlithographic method is capable of fabricating large-scaled nanohoneycomb metal foils (*e.g.*, Figure 2f) not just for Ni but other metals that can be electrodeposited onto an electrode. At present, dealloying methods are widely used to fabricate nanoporous noble metals for electrochemical actuation,[4,9,12] but such methods result in random nanoporous structures. As a result, the charge-induced stresses between neighboring nanoligaments may not be efficiently utilized to produce large actuations, and also the randomly porous structure may restrict the ion diffusion into the pore channels. On the contrary, the template-based nonlithographic method here can result in highly ordered nanohoneycomb arrangements of the pore channels. In addition, the pore size and interpore distance of the porous structure can be controlled in a wide range, by fine-tuning the anodization conditions in the fabrication of the AAO template.[46,48]

Figure S1 shows the scanning electron microscopy (SEM) image of another fabricated bilayered Ni sample with a much thicker ($\sim$1 μm) solid backing layer. This sample was cut into two pieces, which are shown in Figure 2f; the left one has the nanohoneycomb layer facing up, while the right one has the solid Ni layer facing up. The nanohoneycomb Ni layer appears golden in color, in contrast with the usual silvery color of the solid Ni layer. The golden color of the nanohoneycomb Ni may be an intrinsic property due to the ordered metallic structure, such as that in photonic crystals, which can prohibit the propagation of light of a certain frequency range within the photonic band gap.[49,50] It should also be noted that no obvious content of elements that have a golden color can be detected in nanoporous Ni from the energy-dispersive X-ray spectroscopy results (see Figure 2d). X-ray diffraction was performed on the nanohoneycomb Ni layer as well as on the solid Ni backing layer, and as shown in Figure 2f, the result confirms that the nanohoneycomb layer had an fcc crystalline Ni structure almost identical to that of the solid layer of Ni. Compared with solid Ni, however,
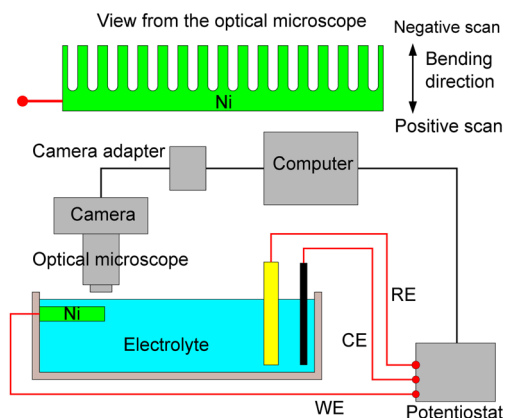

Figure 3. Schematic of an experimental setup for the measurement of the reversible bending of the cantilever-shaped and bilayered Ni upon cyclic charging. During bending of the cantilever, electrochemical properties of the sample are measured by the potentiostat. The top part of the figure illustrates a cross-section view of the sample, which is facing the lens of the optical microscope. The real setup and the sample fixed at the electrochemical cell are shown in Figure S2.

the nanohoneycomb Ni had slight right shifts of the diffraction peaks, indicating a reduction in lattice constant in the nanohoneycomb Ni. From Bragg's law, the lattice constant of the nanoporous Ni was calculated to be 3.5182 Å, which is about 0.105% smaller than that of bulk Ni (3.5219 Å); see Table S1. Therefore, in the absence of excess electric charges, contraction strain already exists within the nanoporous Ni. This is in accordance with Ibach's model, in which the surface electrons redistribute into the regions between the surface atoms, resulting in an increase of the bond strength and a reduction of the equilibrium interatomic distance.[43,44]

Electrochemical Actuation in Bilayered Nanohoneycomb/Solid Ni. For electrochemical characterization of the bilayered nanohoneycomb/solid Ni foils, as shown in Figures 3 and S2, an *in situ* setup was constructed. One end of the Ni foil was fixed at the wall of the electrochemical cell, while the other end could move freely. During charging, any slight movement of the foil's free end was directly observed and magnified by the optical microscope, captured by a CCD camera, and then recorded as videos by a computer. The displacement of the free end was measured from the videos. The images observed by the optical microscope correspond to the cross-section of the bilayered Ni as shown in the top part of Figure 3, and the real situation is shown in Figure S2. At the same time, the electrochemical properties of the sample were measured by the potentiostat in order to understand the actuation mechanism.

Figure 4 shows typical relationships of the free-end displacement of a bilayered Ni foil against time under cyclic potential actuations, while the corresponding current during the potential scanning is shown in
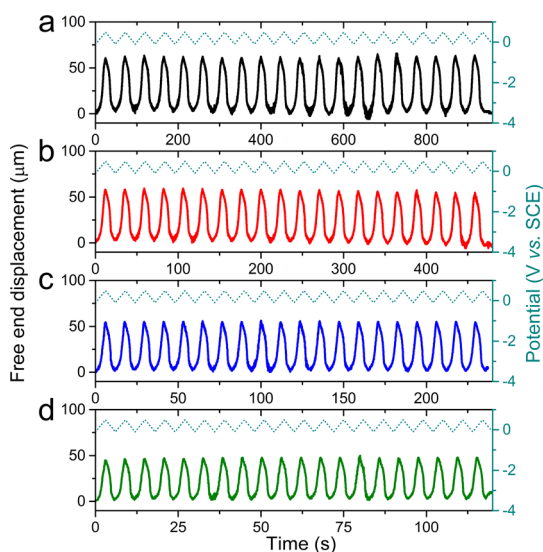
Figure 4. Displacement of the free end of a bilayered Ni foil in 1 M NaOH electrolyte during the measurement of cyclic voltammetry shown in Figure 5a. The potential scan rates are (a) 25 mV/s, (b) 50 mV/s, (c) 100 mV/s, and (d) 200 mV/s, respectively. The corresponding videos for Figures 4c and d are provided in the Supporting Information. The potential against time relationships are represented by dash lines in the top part of the figures. More measurements at scan rates from 75 to 500 mV/s are shown in Figure S3. Sample size: 10 mm × 3 mm × 3.0 μm (porous layer 2.0 μm + solid layer 1.0 μm thick).

Figure 5a. Twenty repeating potential loops were applied at each scan rate of 25, 50, 100, and 200 mV/s as shown in Figure 4a−d, respectively. For the same sample, more measurements under different scan rates ranging from 75 to 500 mV/s are shown in Figure S3. For all of the cases in Figures 4 and S3, highly reversible displacements were clearly observed under the cyclic potential actuation (dash lines at the top part of the subfigures). At different scan rates, the displacement against time curves are very similar in shape, and the varying tendency is in accordance with the corresponding potentials, except the magnitude of the displacement, which is scan-rate dependent (discussed later in Figure 7). Thus, the actuation of the bilayered Ni can be well controlled by the scan rate and potential. In Figure 4, during positive potential scanning, the bilayered cantilever bends toward the solid Ni layer, which indicates expansion straining taking place in the nanoporous layer. On the contrary, the strain tends to be contraction in the nanoporous layer during negative potential scan. As shown in the Figure 5a, during the repeating cyclic actuations of the cantilever, the corresponding cyclic voltammograms are highly overlapping, in accordance with the high reversibility of the displacements shown in Figures 4 and S3.
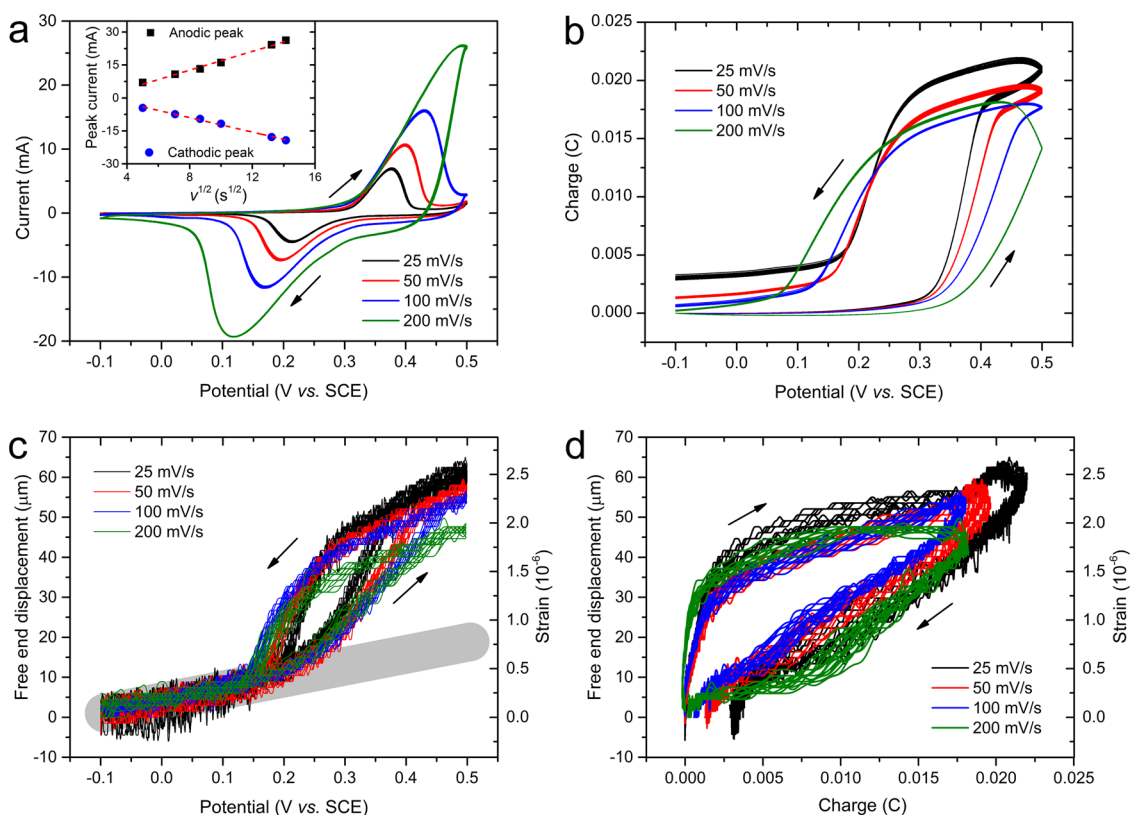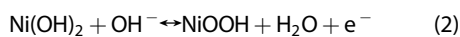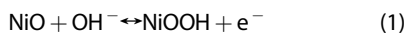

Figure 5. (a) Cyclic voltammograms of the bilayered Ni foil measured between −0.1 to 0.5 V (*vs* SCE), at the scan rates of 25, 50, 100, and 200 mV/s, respectively. Twenty loops are applied under each scan rate, which correspond to the 20 displacement cycles in Figure 4. The inset figure shows linear relationships between the anodic/cathodic current peaks against the square root of the scan rate *v*. (b) Charge against potential relationships under different scan rates, which are integrated from the cyclic voltammograms. (c, d) Free-end displacement (left axis) and strain (right axis) against potential and charge, respectively. The gray band in (c) represents a linear trend between strain and potential. The strain and charge at −0.1 V are used as the reference points (zero points).
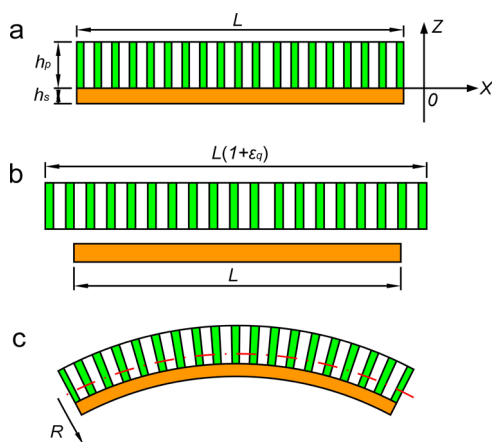
Figure 6. (a) Schematic of the bilayered Ni foil without electric charging, with porous layer thickness h_p and solid layer thickness h_s. (b) Upon charging q, charge-induced intrinsic strain ε_q is produced within the porous layer. (c) Due to the constraint by the solid layer, the bilayered foil bends upon charging, with radius of curvature R.

In Figure 5a, the anodic and cathodic current peaks of cyclic voltammograms indicate a pseudocapacitive behavior, indicating faradaic charge transfer by means of reversible redox reactions.[42] The electrochemical capacitance at the electrode/electrolyte interface is mainly contributed from the pseudocapacitance rather than the electrostatic capacitance of the double layer. From the literature,[51−53] the anodic and cathodic currents peak in the vicinity of 0.4 and 0.1 V, respectively, which can be attributed to the oxidation and reduction of the redox couple of Ni(II)/Ni(III). Ni(II) comes from the passive film along the surface of the Ni electrode, possibly in the form of bilayered NiO/Ni(OH)$_2$,[54−56] while the Ni(III) is in the form of NiOOH.[51] Thus, the possible redox reactions are

$$NiO + OH^- \leftrightarrow NiOOH + e^- \quad (1)$$

$$Ni(OH)_2 + OH^- \leftrightarrow NiOOH + H_2O + e^- \quad (2)$$

With increasing scan rate, the anodic and cathodic peaks shift toward positive and negative potential directions, respectively, because of the limitation of the OH$^-$ diffusion rate in order to satisfy electronic neutralization during the redox reactions.[57] From the inset in Figure 5a, both the anodic and cathodic current peaks exhibit linear relationships with the square root of the scan rate, which satisfies the Cottrell equation,[52,58] $i = nFAC\sqrt{D}/(\pi t)^{1/2} = av^{1/2}$, where n is the number of electrons transferred during redox reactions, F is the Faradaic constant, A is the effective area of the electrode, C is the concentration of the electrolyte, D is the diffusion coefficient, t is the time, a is a collection constant, and v is the scan rate. This indicates that the charge transfer due to faradic reactions at the electrode surface is faster than the ion diffusion to the electrode surface, and the current is limited by the latter process.

As shown in Figure 5b, by regarding the amount of charges at the −0.1 V as a reference point (zero charge), the charges under different potentials are obtained by integrating the cyclic voltammograms in Figure 5a. From the free-end displacement in Figure 4, the displacement against potential and charge relationships are shown in Figure 5c and d, respectively. Note that slight fluctuations in displacement shown in Figure 5c and d are vibrations due to the slight environmental noise.

As illustrated in Figure 6a and b, upon charging, the charge-induced stress within the porous layer results in a biaxial strain ε_p there. Due to the constraint by the underlying solid layer, bending of the bilayered foil takes place, as shown in Figure 6c. Here, ε_p is the intrinsic strain of the porous layer due to charging; it arises from the charging of the actuating porous layer, although in the current experimental setup, it is measured by the bending of the bilayered foil. This situation is similar to the thermal-induced bending of bi- or multilayered films due to differences in thermal expansivities.[59] Here, the charge-induced strain ε_p is calculated analytically based on a method developed from Hsueh[60] (see the Supporting Information for detailed derivation):

$$\varepsilon_q = \frac{1}{R} \frac{E_p^2 h_p^4 (1-\nu_s)^2 + E_s^2 h_s^4 (1-\nu_p)^2 + 2E_p E_s h_p h_s (2h_p^2 + 2h_s^2 + 3h_p h_s)(1-\nu_p)(1-\nu_s)}{6E_p E_s h_p h_s (h_p + h_s)(1-\nu_p)(1-\nu_s)} \quad (3)$$

where the subscripts "p" and "s" indicate parameters for the porous and solid layers, respectively; E is Young's modulus; ν is Poisson's ratio, h is the layer thickness, and R is the radius of curvature of the bent bilayer. Here, the porous layer is regarded as transversely isotropic with an effective in-plane Young's modulus E_p, according to Gibson and Ashby:[61]

$$E_p \approx E_s C \left(\frac{\rho_p}{\rho_s} \right)^2 \quad (4)$$

where E_s = 205 GPa is the Young's modulus of the electroplated solid Ni,[62,63] C is a constant related to the porous geometry, and ρ_p and ρ_s are the densities of the porous and solid Ni, respectively. Details of the parameters used can be found in the Supporting Information. From eq 3, the charge-induced strain ε_p is linearly proportional to the curvature of the bent bilayer by a factor related to the mechanical and geometrical properties of the bilayer. Due to the large difference between the length L and thickness ($h_s + h_p$) of the present bilayer, the radius of curvature is given by $R \approx L^2/(2\delta)$ from the cantilever geometry, where δ is the free-end displacement of the bilayered cantilever measured in Figure 4. The values of ε_q are also plotted as the right axis of Figure 5c and d.
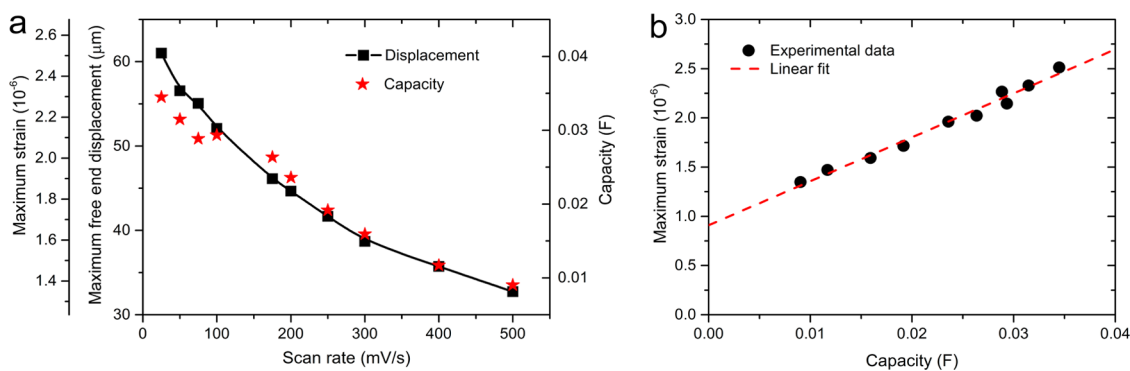
Figure 7. (a) Maximum values of the free-end displacement and strain against potential scan rates. In the same figure, the electrochemical capacity is calculated by eq 5 from the cyclic voltammograms shown in Figures 5a and S3. (b) Maximum strain against capacity relationship.

As the potential increases from −0.1 V to 0.15 V, the free-end displacement (or strain) linearly increases from 0 μm to ∼10 μm (Figure 5c), which corresponds to the linear increase of charges in Figure 5b. Within this lower potential regime, the strain is induced by the accumulated charges at the capacitive electrochemical double layer, within which the charges linearly depend on the potential. However, the linear tendency, as noticed by the gray region in Figure 5c, was not maintained at higher potentials from 0.15 to 0.5 V, within which the majority increase of the displacement takes place from ∼10 to ∼60 μm. Accordingly, the charges increase much faster with potential in Figure 5b. The relatively higher potential regime corresponds to the redox reactions, as indicated by the current peaks in Figure 5a. From Figure 5c, within the whole potential region, the majority of the strain (∼67%) is contributed from the faradic redox reactions, while the rest (∼33%) is due to the charge accumulation at the capacitive double layer.

During the positive scan, the expansion strain may arise from volume expansion due to the oxidation of NiO into NiOOH according to eq 1 or due to the lattice mismatching between Ni(II) and Ni(III). For instance, on oxidation from NiO to NiOOH, the volume expansion ratio (the Pilling−Bedworth ratio[64]) is about $1.69 = [(58.69 + 2 \times 15.99 + 1) \text{ g}/4.84 \text{ g cm}^{-3}]/[(58.69 + 15.99) \text{ g}/6.67 \text{ g cm}^{-3}]$, which corresponds to 69% increase of the volume. At a certain scan rate, in Figure 5c and d, the curves between positive and negative scans do not overlap with each other due to the faradic redox reactions, and this behavior is remarkably different from the nonfaradic process in the capacitive electrochemical double layers, in which the strain increases almost linearly with potential (as well as charges) along the same line for both positive and negative scans; see, for example, Figure 2e of ref 36 and Figure 2c of ref 12. In addition, from Figure 5c and d, the strain depends more sensitively on the scan rate at the higher potential regime above 0.15 V, where redox reactions take place, compared with the lower

potential regime, where purely capacitive charging takes place.

Figure 7a shows that the maximum strain obtained at a certain scan rate decreases exponentially with the scan rate. At the lowest scan rate of 25 mV/s in the present tests, the maximum strain is about 2.5×10^{-6} and the corresponding strain energy (work density) is $W_q = 0.5 E_p \varepsilon_q^2 \approx 0.3$ J/m^3. Due to the small strain, the work density is much less than that of the previous nanoporous noble metals, e.g., 90 kJ/m^3 for Pt reported by Weissmüller et al.[12] The reason for the small strain may include the following: (i) the porosity of our nanoporous Ni is ∼23%, while the porosity of Pt is ∼90%,[12] and as a result, the present material has a much smaller surface-area-to-volume ratio, which can lead to a significant decrease of the strain amplitude and increase of the effective bulk modulus;[12] (ii) the lowest potential scan rate among our tests is about 25 times faster than that in the work of Weissmüller et al.[12] (e.g., ∼1 mV/s),[12] so that in the present experiments the strain amplitude may not be fully developed. However, also due to the lower porosity of the nanoporous Ni, it has a much higher Young's modulus (∼108 GPa; see Supporting Information) than the nanoporous noble metals (e.g., ∼9 GPa for Pt[12] and ∼11 GPa for Au),[65] meaning a more rigid structure. In addition, under the highest potential scan rate used in our tests (500 mV/s), it only takes about 1.2 s to reach a strain of ∼1.3×10^{-6} (with a strain rate ∼10^{-6}/s), while for the existing nanoporous noble metals, such as nanoporous Pt, actuated within the capacitive double-layer region (Figure 2 of ref 12), the strain rate was ∼10^{-7}/s under the potential scan rate ∼1 mV/s.

From Figure 7a, the electrochemical capacity decreases with the scan rate along a trend similar to the displacement. Here, the electrochemical capacity was calculated as[52,53]

$$C = \frac{1}{v\Delta V} \int_{V_a}^{V_c} i(V) \, dV \qquad (5)$$

where $\Delta V = V_a - V_c$ is the applied potential window, V_a is the end of the anodic potential, V_c is the end of the
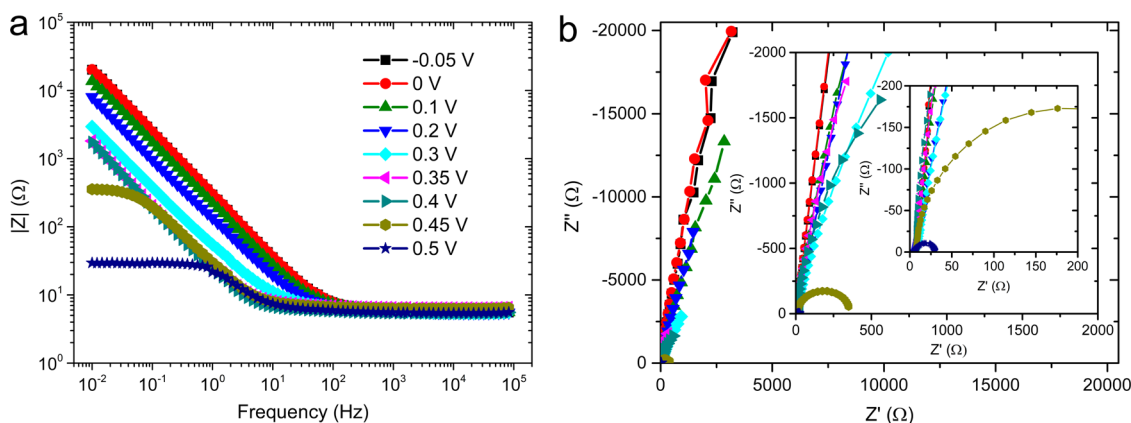
Figure 8. Electrochemical impedance spectroscopy for the bilayered nanohoneycomb/solid Ni in 1 M NaOH electrolyte. (a) Bode plot showing the frequency dependence of the impedance magnitude $|Z|$. (b) Nyquist plot showing the relationship between the real part (Z') and imaginary part (Z'') of the impedance. Each curve corresponds to different potentials (vs SCE) as noticed in (b). Inset figures show enlarged plot at the high-frequency regions. Sample size: 10 mm × 2 mm × 3.0 μm (porous layer 2.0 μm + solid layer 1.0 μm thick).

cathodic potential, ν is the potential scan rate, and i is the current obtained from the cyclic voltammograms in Figures 5 and S3. Because the current is ion-diffusion-controlled (see inset of Figure 5a), a faster scan rate limits the ion diffusion into the nanoporous structures, which restricts the rate of redox reactions. As a result, the capacity, which is related to the amount of charges that can be stored at the interface, decreases with the scan rate.

Note that if C in eq 5 is divided by the mass of the sample, it becomes the specific capacitance with regard to supercapacitors.[52,53,57] The decreasing relationship between the specific capacitance and the potential scan rate has been reported in Ni(OH)$_2$/graphene- or NiO-based supercapacitors.[52,53,57] Also, on the topic of electrochemical actuators, the decreasing tendency between strain and scan rate has been reported in nanoporous platinum[66] and gold/polyaniline actuators.[67] Here, we have demonstrated that the maximum strain, which can be reached under a certain potential scan rate, increases linearly with the electrochemical capacity, with a slope of $d\varepsilon_{max}/dC = 4.5 \times 10^{-5}$ F^{-1}, as shown in Figure 7b. Linear extrapolation of the graph indicates a considerable strain ($\varepsilon_{max,C=0} \approx 9.1 \times 10^{-7}$) at zero capacity. Note that the strain used here refers to the strain at -0.1 V (i.e., ε_{ref}), as shown in Figure 5c and d. Thus, $\varepsilon_{max} = \varepsilon_{ref} + \varepsilon_{real}$, where ε_{real} means the real strain of the material by referring to its strain-free condition. At zero capacity, the real stain should also be zero, i.e., $\varepsilon_{real,C=0} = 0$. Thus, $\varepsilon_{ref} = \varepsilon_{max,C=0}$, which indicates that at -0.1 V potential the real strain is about 9.1×10^{-7}. This linear relationship also indicates that electrochemical capacitors (supercapacitors) with a higher capacity can lead to a larger magnitude of the charge-induced deformation during charging/discharging processes. Although nanoporous materials with larger electrochemical capacity are preferable for both electrochemical actuator and supercapacitor

applications, they can also result in a larger extent of degradation due to the corresponding larger strain. The linear relationship between the maximum strain and the electrochemical capacity may be equally significant in the material design for both electrochemical actuators and supercapacitors.

Electrochemical impedance spectroscopy was performed in order to further understand the electrochemical processes that take place at the bilayered Ni electrode/electrolyte interface upon triggering by different potentials from -0.05 to 0.5 V (vs SCE). The Bode plot in Figure 8a shows that, within the low-frequency (<10 Hz) regime, the magnitude of the impedance gradually decreases with potential increasing from -0.05 V to 0.4 V, but decreases much more quickly with potential increasing from 0.4 V to 0.5 V. The first decreasing trend is likely attributed to the enhanced ion diffusion under higher potentials, while the latter, faster decreasing trend is attributed to the faradic reactions that take place once the electric field at the interface is high enough to overcome the potential barriers.[68] Accordingly, in the low-frequency regime, the Nyquist plot in Figure 8b clearly shows a characteristic semicircle under 0.45 V, which indicates that the impedance is dominated by charge transfer resistance of the faradic reactions, which is the diameter of the semicircle. The potential around 0.45 V corresponds to a region where the anodic current peaks appear in the cyclic voltammograms in Figure 5a. Thus, the impedance spectroscopy confirms that the anodic peak originates from faradic reactions. On the contrary, under lower potentials, such as -0.05, 0, and 0.1 V, linear relationships between Z' and Z'' were observed in the Nyquist plot. This indicates that the impedance is dominated by ion diffusion, namely, the so-called Warburg impedance.[69] In particular, the Z' vs Z'' plots are close to vertical lines, which correspond to the impedance diagram of the purely capacitive electrochemical double
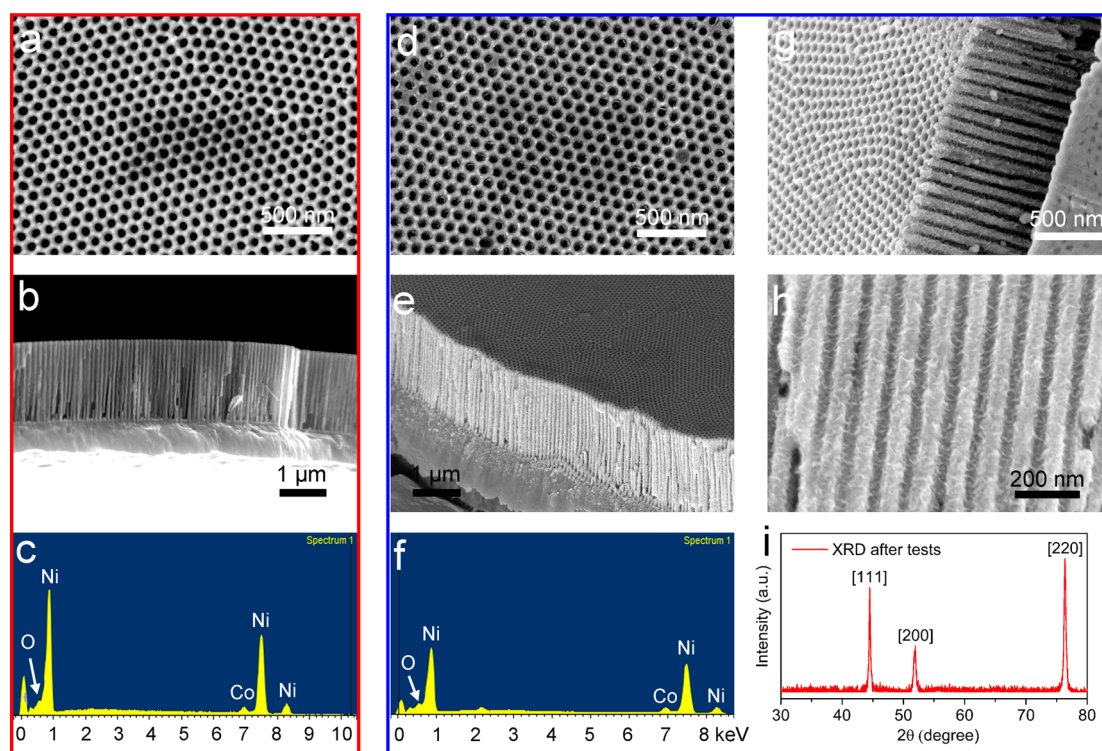
Figure 9. Bilayered nanohoneycomb/solid Ni with a 2 μm thick porous layer and a 1 μm thick solid layer. (a−c) As synthesized before electrochemical tests; (d−i) after the series of electrochemical actuation tests in Figures 4 and S3. (a, b, d, e, g, h) SEM images of the sample: top view (a, d), cross-sectional view (b, e), and (g, h) magnified cross-sectional views for (e). (c, f) Energy-dispersive X-ray spectroscopy showing the oxygen content increasing from ∼2.1 wt % to ∼4.1 wt % after the electrochemical tests. (i) XRD of the sample after electrochemical tests showing that the sample is still crystalline Ni, and any possible oxidation products are too little to be detected.

layer. Thus, the impedance spectroscopy confirms that the nonfaradic charging at the double layer is the dominating process within the lower potential region. From Figure 5c, the nonfaradic process, which results in the linear increase of the strain with increasing potential, contributes only about 33% of the maximum strain at the positive potential end. Thus, it is the faradic redox reactions that contribute to the majority part of the strain.

In order to check the reliability of the bilayered nanohoneycomb/solid Ni, the sample is characterized before and after a series of electrochemical actuation tests, including more than 500 cyclic actuation loops within the potential range of [−0.1, 0.5] V, at different scan rates varying from 25 to 500 mV/s. By comparing the SEM top views shown in Figure 9a and d, the nanohoneycomb architecture within the porous Ni is well maintained after the actuation tests. The average pore diameters before and after the tests are all about 50 nm. By comparing the cross-sectional views of the bilayered Ni shown in Figure 9b and e, the pore channels remain hollow and straight after the actuation tests, without any sign of blocking of the channels by possible reaction products or without collapse of the channels due to possible reduction of the very thin pore walls (∼46 nm). Specifically, from the magnified cross-sectional views shown in Figure 9g and h, the

roughness of the pore channels increases slightly after the actuation tests, compared with the relatively smooth condition before the tests (see also Figure 2e). Actually, this type of rough surface was also noted in Ni nanowires by only immersing into 1 M NaOH without any electric actuation, as shown in Figure S4. The Ni nanowires were synthesized by the same electrochemical deposition condition, and the roughness seen in Figure S4 was formed immediately after immersion in NaOH and remained as such even after immersion in NaOH for several days. The rough surface here is likely the passive film of Ni(II), the thickness of which increases with electric potential, in the range from 1 to 4 nm according to XPS analysis,[54] ellipsometry,[55] and coulometry.[56] This is also supported by EDX results, which show a slight increase of the oxygen content within the cross-section of the bilayered Ni, from ∼2.6 wt % to ∼4.1 wt % after the actuation tests, as shown in Figure 9c and f. However, the XRD results exhibit only characteristic peaks of face-centered-cubic Ni, which are very similar to those of the nanoporous Ni before the electrochemical actuation tests, as shown in Figure 2g. Thus, both the nanohoneycomb architecture and the crystal structure are mechanically and chemically stable after a series of electrochemical actuation tests, which in turn guarantees the stable and reversible displacements of the sample during

cyclic actuations, as shown in Figures 4 and S3. This reversibility originates from the reversible Ni(II)/Ni(III) redox couple at the surface of the nickel electrode, while the nickel underneath the surface oxide provides an efficient conductive background for the redox reactions. During the charging/discharging processes, the high reliability and charge capacity of the Ni(II)/Ni(III) redox couple have been widely appreciated in the area of supercapacitors,[52,57,70] and here, we have demonstrated that such properties are beneficial for the application as electrochemical actuators with a nanohoneycomb structure.

CONCLUSIONS

This work has shown that nickel-based electrochemical actuators, in the form of bilayered nanohoneycomb/solid cantilevers, exhibit reversible and stable strain upon cyclic potential triggering by less than 0.5 V. The reversible strain is mainly due to the pseudocapacitive processes by means of reversible redox reactions. The nanohoneycomb structure in nickel was fabricated from self-ordered anodic aluminum oxide by a two-template-based method. This method should also be applicable to fabricate ordered nanoporous structures of other metals for electrochemical actuator applications in a cost-effective way. Electrochemical properties of the Ni bilayered nanohoneycomb/solid cantilevers were characterized *in situ* during their actuation. Their actuation strain varies nonlinearly with the applied potential and charge due to the redox reactions, while the strain exponentially decreases with potential scan rate due to the ion diffusion. The maximum strain, which can be achieved at a certain scan rate within a potential range, increases linearly with the electrochemical capacity.

METHODS

Fabrication Methods. Aluminum foils (99.99%, 0.5 mm in thickness and 1 in. in diameter) were annealed under vacuum ($\sim 10^{-5}$ Torr) at 500 °C for 48 h, then mechanically polished with 1200, 2400, and 4000 grit SiC sandpapers and 6 μm, 1 μm diamond pastes in succession, and finally electropolished in a solution mixture of $HClO_4$ (60 wt %) and C_2H_5OH in 1:4 ratio by volume under 20 V at about -10 °C for 2 min.

To produce the anodic aluminum oxide (AAO) templates, the Al foils were anodized by a high-acid-concentration and high-temperature anodization condition that we previously have established.[46] Such an HHA condition can shorten the anodization time from the conventional 2 days to only 2 to 3 h, while the formed porous structures have much better ordering quality as well as mechanical stability with high aspect ratios of the pore channels.[46] The Al foils were anodized under the condition of 0.9 M $H_2C_2O_4$, 40 V, 20 °C, and 3 h, and then the formed AAO was selectively removed from the Al substrate by a solution of H_2CrO_4, H_3PO_4, and H_2O in a ratio of 1.8:6:92.2 by weight at 60 °C. Then, a second anodization step was conducted under the same conditions as in the first step for 5 min. After that, the pores of AAO were further opened up in 5 wt % H_3PO_4 for 30 min under room temperature.

The top surface of AAO was then sputtered with a nanoscale layer of Au. Polymer powder (resin, SepciFast, Struers Inc.) was thermally molded into the channels of the AAO nanohoneycomb structure by a hot-mount machine (Struers Inc.). The molding condition was 180 °C for 5 min under 15 kN load, followed by water cooling for 9 min. The Al substrate was then selectively dissolved by a solution of $CuCl_2$ and HCl (100 mL of 38% HCl + 100 mL of H_2O + 3.4 g of $CuCl_2 \cdot 2H_2O$), and then the alumina existing between the polymer pillars was selectively dissolved by saturated NaOH solution under low temperatures (~ -2 °C) in order to avoid the tangling together of the polymer pillars. Electrodeposition of Ni was performed under a constant current density of -10 mA/cm^2, with an electrolyte of 0.15 M $NiSO_4$ + 0.6 M HBO_3 at room temperature. Afterward, the inverse polymer template was electively dissolved by acetone for about 2 days.

Characterization Methods. Scanning electron microscopy examination was carried out in a Hitachi S-4800 field-emission microscope and a LEO 1530 field-emission microscope. Energy-dispersive X-ray spectroscopy was carried out also in the LEO 1530 field-emission microscope. The crystalline structure of Ni was analyzed by X-ray diffraction in a Bruker D8 diffractometer (Cu Kα).

To measure the electrochemical actuation of the bilayered nanohoneycomb/solid Ni cantilever, an electrochemical cell was placed on the sample stage of an optical microscope (Olympus Co.). The work electrode was bilayered Ni, which had one end fixed on the wall of the electrochemical cell, while the other end could move freely. The sample was immersed just underneath 1 M NaOH electrolyte, with its free end observed by optical microscope. Potentiostat measurements were made under a three-electrode mode by a potentiostat (LK2006A, LANLIKE Co.), with a Pt wire as the counter electrode and SCE (saturated calomel electrode) as the reference electrode. A CCD camera (CCD-IRIS, Color Video Camera, Sony Co.) was connected to the optical microscope by a microscope attachment (WV-9005, Matsushita Comm. Industrial Co. Ltd.) in order to capture the magnified movement of the free end of the sample. The signal from the camera was channeled to a camera adapter (model CMA-D7CE, Sony Co.) and was recorded as a movie by computer. By using this setup, any significant movement of the free end of the sample, which was located at the focal point of the objective lens, can be enlarged and recorded in real time.

Electrochemical impedance spectroscopy (EIS) measurement was also conducted on an electrochemical workstation (660D, CH Instruments Inc., USA), with SCE as the reference electrode and Pt as the counter electrode, in 1 M NaOH solution. EIS was performed at different dc polarizations (*vs* SCE) under an ac perturbation (5 mV sin wave), over a frequency range from 10^5 Hz down to 10^{-2} Hz.

Conflict of Interest: The authors declare no competing financial interest.

Supporting Information Available: SEM images corresponding to Figure 2f; X-ray diffraction data analysis corresponding to Figure 2g; photograph of the experimental setup corresponding to Figure 3; two videos corresponding to Figure 4c and d; SEM image for nanostructured Ni immersed in 1 M NaOH electrolyte for 5 days. This material is available free of charge *via* the Internet at http://pubs.acs.org.

REFERENCES AND NOTES

1. Mirfakhrai, T.; Madden, J. D. W.; Baughman, R. H. Polymer Artificial Muscles. *Mater. Today* **2007**, *10*, 30–38.
2. Li, D. B.; Paxton, W. F.; Baughman, R. H.; Huang, T. J.; Stoddart, J. F.; Weiss, P. S. Molecular, Supramolecular,

and Macromolecular Motors and Artificial Muscles. *MRS Bull.* **2009**, *34*, 671–681.

3. Qu, L. T.; Peng, Q.; Dai, L. M.; Spinks, G. M.; Wallace, G. G.; Baughman, R. H. Carbon Nanotube Electroactive Polymer Materials: Opportunities and Challenges. *MRS Bull.* **2008**, *33*, 215–224.

4. Jin, H. J.; Weissmüller, J. Bulk Nanoporous Metal for Actuation. *Adv. Eng. Mater.* **2010**, *12*, 714–723.

5. Weissmüller, J.; Newman, R. C.; Jin, H. J.; Hodge, A. M.; Kysar, J. W. Nanoporous Metals by Alloy Corrosion: Formation and Mechanical Properties. *MRS Bull.* **2009**, *34*, 577–586.

6. Zhang, Q.; Bharti, V.; Zhao, X. Giant Electrostriction and Relaxor Ferroelectric Behavior in Electron-Irradiated Poly-(Vinylidene Fluoride-Trifluoroethylene) Copolymer. *Science* **1998**, *280*, 2101–2104.

7. Baughman, R. H. Conducting Polymer Artificial Muscles. *Synth. Met.* **1996**, *78*, 339–353.

8. Hunter, I. W.; Lafontaine, S. A Comparison of Muscle with Artificial Actuators. *Solid-State Sensor and Actuator Workshop, 1992. 5th Technical Digest., IEEE* **1992**, 178–185.

9. Jin, H. J.; Wang, X. L.; Parida, S.; Wang, K.; Seo, M.; Weissmüller, J. Nanoporous Au-Pt Alloys as Large Strain Electrochmical Actuators. *Nano Lett.* **2010**, *10*, 187–194.

10. Detsi, E.; Selles, M. S.; Onck, P. R.; De Hosson, J. T. M. Nanoporous Silver as Electrochemical Actuator. *Scr. Mater.* **2013**, *69*, 195–198.

11. Jin, H. J.; Weissmüller, J. A Material with Electrically Tunable Strength and Flow Stress. *Science* **2011**, *332*, 1179–1182.

12. Weissmüller, J.; Viswanath, R. N.; Kramer, D.; Zimmer, P.; Würschum, R.; Gleiter, H. Charge-Induced Reversible Strain in a Metal. *Science* **2003**, *300*, 312–315.

13. Detsi, E.; Punzhin, S.; Rao, J.; Onck, P. R.; De Hosson, J. T. M. Enhanced Strain in Functional Nanoporous Gold with a Dual Microscopic Lengh Scale Structure. *ACS Nano* **2012**, *6*, 3734–3744.

14. Oh, J.; Kozlov, M. E.; Kim, B. G.; Kim, H. K.; Baughman, R. H.; Hwang, Y. H. Preparation and Electrochemical Characterization of Porous SWNT-PPy Nanocomposite Sheets for Supercapacitor Applications. *Synth. Met.* **2008**, *158*, 638–641.

15. Baughman, R. H.; Cui, C.; Zakhidov, A. A.; Lqbal, Z.; Barisci, J. N.; Spinks, G. M.; Wallace, G. G.; Mazzoldi, A.; Rossi, D. D.; Rinzler, A. G.; *et al*. Carbon Nanotube Actuators. *Science* **1999**, *284*, 1340–1344.

16. Aliev, A. E.; Oh, J. Y.; Kozlov, M. E.; Kuznetsov, A. A.; Fang, S. L.; Fonseca, A. F.; Ovalle, R.; Lima, M. D.; Haque, M. H.; Gartstein, Y. N.; *et al*. Giant-Stroke, Superelastic Carbon Nanotube Aerogel Muscles. *Science* **2009**, *323*, 1575–1578.

17. Baughman, R. H. Playing Nature's Game with Artificial Muscles. *Science* **2005**, *308*, 63–65.

18. Baughman, R. H.; Zakhidov, A. A.; de Heer, W. A. Carbon Nanotubes - the Route Toward Applications. *Science* **2002**, *297*, 787–792.

19. De Volder, M. F. L.; Tawfick, S. H.; Baughman, R. H.; Hart, A. J. Carbon Nanotubes: Present and Future Commercial Applications. *Science* **2013**, *339*, 535–539.

20. Chen, L. Z.; Liu, L.; Kim, L.; Meng, C. Z.; Hu, C. H.; Wang, J. P.; Fan, S. S. High-Performance, Low-Voltage, and Easy-Operable Bending Actuator Based on Aligned Carbon Nanotube/Polymer Composites. *ACS Nano* **2011**, *5*, 1588–1593.

21. Shao, L. H.; Biener, J.; Kramer, D.; Viswanath, R. N.; Baumann, T. F.; Hamza, A. V.; Weissmüller, J. Electrocapillary Maximum and Potential of Zero Charge of Carbon Aerogel. *Phys. Chem. Chem. Phys.* **2010**, *12*, 7580–7587.

22. Kim, J.; Jeon, J. H.; Kim, H. J.; Lim, H.; Oh, I. K. Durable and Water-Floatable Ionic Polymer Actuator with Hydrophobic and Asymmetrically Laser-Scribed Reduced Graphene Oxide Paper Electrodes. *ACS Nano* **2014**, *8*, 2986–2997.

23. Liang, J. J.; Huang, L.; Li, N.; Huang, Y.; Wu, Y. P.; Fang, S. L.; Oh, J. Y.; Kozlov, M.; Ma, Y. F.; Li, F. F.; *et al*. Electromechanical Actuator with Controllable Motion, Fast Response Rate, and High-Frequency Resonance Based on Graphene and Polydiacetylene. *ACS Nano* **2012**, *6*, 4508–4519.

24. Xie, X. J.; Qu, L. T.; Zhou, C.; Li, Y.; Zhu, J.; Bai, H.; Shi, G. Q.; Dai, L. M. An Asymmetrically Surface-Modified Graphene Film Electrochemical Actuator. *ACS Nano* **2010**, *4*, 6050–6054.

25. Baughman, R. H. Muscles Made from Metal. *Science* **2003**, *300*, 268–269.

26. Detsi, E.; Onck, P. R.; De Hosson, J. T. M. Electrochromic Artificial Muscles Based on Nanoporous Metal-Polymer Composites. *Appl. Phys. Lett.* **2013**, *103*, 193101-1–193101-3.

27. Shao, L. H.; Biener, J.; Jin, H. J.; Biener, M. M.; Baumann, T. F.; Weissmuller, J. Electrically Tunable Nanoporous Carbon Hybrid Actuators. *Adv. Funct. Mater.* **2012**, *22*, 3029–3034.

28. Volkert, C. A.; Lilleodden, E. T.; Kramer, D.; Weissmuller, J. Approaching the Theoretical Strength in Nanoporous Au. *Appl. Phys. Lett.* **2006**, *89*, 061920-1–061920-3.

29. Biener, J.; Hodge, A. M.; Hayes, J. R.; Volkert, C. A.; Zepeda-Ruiz, L. A.; Hamza, A. V.; Abraham, F. F. Size Effects on the Mechanical Behavior of Nanoporous Au. *Nano Lett.* **2006**, *6*, 2379–2382.

30. Jin, H. J.; Kurmanaeva, L.; Schmauch, J.; Rosner, H.; Ivanisenko, Y.; Weissmuller, J. Deforming Nanoporous Metal: Role of Lattice Coherency. *Acta Mater.* **2009**, *57*, 2665–2672.

31. Hakamada, M.; Takahashi, M.; Furukawa, T.; Mabuchi, M. Coercivity of Nanoporous Ni Produced by Dealloying. *Appl. Phys. Lett.* **2009**, *94*, 153105-1–153105-3.

32. Hayes, J. R.; Hodge, A. M.; Biener, J.; Hamza, A. V.; Sieradzki, K. Monolithic Nanoporous Copper by Dealloying Mn-Cu. *J. Mater. Res.* **2006**, *21*, 2611–2616.

33. Min, U. S.; Li, J. C. M. The Microstructure and Dealloying Kinetics of a Cu-Mn Alloy. *J. Mater. Res.* **1994**, *9*, 2878–2883.

34. Sun, L.; Chien, C. L.; Searson, P. C. Fabrication of Nanoporous Nickel by Electrochemical Dealloying. *Chem. Mater.* **2004**, *16*, 3125–3129.

35. Wang, X. G.; Qi, Z.; Zhao, C. C.; Wang, W. M.; Zhang, Z. H. Influence of Alloy Composition and Dealloying Solution on the Formation and Microstructure of Monolithic Nanoporous Silver through Chemical Dealloying of Al-Ag Alloys. *J. Phys. Chem. C* **2009**, *113*, 13139–13150.

36. Kramer, D.; Viswanath, R. N.; Weissmüller, J. Surface-Stress Induced Macroscopic Bending of Nanoporous Gold Cantilevers. *Nano Lett.* **2004**, *4*, 793–796.

37. Biener, J.; Wittstock, A.; Baumann, T. F.; Weissmüller, J.; Baumer, M.; Hamza, A. V. Surface Chemistry in Nanoscale Materials. *Materials* **2009**, *2*, 2404–2428.

38. Jin, H. J.; Weissmuller, J. Bulk Nanoporous Metal for Actuation. *Adv. Eng. Mater.* **2010**, *12*, 714–723.

39. Weissmuller, J.; Duan, H. L. Cantilever Bending with Rough Surfaces. *Phys. Rev. Lett.* **2008**, *101*, 146102-1–146102-4.

40. Wang, Y.; Weissmuller, J.; Duan, H. L. Mechanics of Corrugated Surfaces. *J. Mech. Phys. Solids* **2010**, *58*, 1552–1566.

41. Vukovic, I.; Punzhin, S.; Vukovic, Z.; Onck, P.; De Hosson, J. T. M.; Brinke, G. Supramolecular Route to Well-Ordered Metal Nanofoams. *ACS Nano* **2011**, *5*, 6339–6348.

42. Conway, B. E.; Pell, W. G. Double-Layer and Psedocapacitance Types of Electrochemical Capacitors and Their Applications to the Development of Hybrid Devices. *J. Solid State Electrochem.* **2003**, *7*, 637–644.

43. Ibach, H. The Role of Surface Stress in Reconstruction, Epitaxial Growth and Stabilization of Mesoscopic Structures. *Surf. Sci. Rep.* **1997**, *29*, 195–263.

44. Saane, S. S. R.; De Hosson, J. T. M.; Onck, P. R. Atomistic Modelling of Charge-Induced Deformation of Gold Nanowires. *Model. Simul. Mater. Sci. Eng.* **2013**, *21*, 055024-1–055024-13.

45. Weissmüller, J.; Cahn, J. W. Mean Stresses in Microstructures Due to Interface Stresses: A Generalization of a Capillary Equation for Solids. *Acta Mater.* **1997**, *45*, 1899–1906.

46. Cheng, C.; Ngan, A. H. W. Fast Fabrication of Self-Ordered Anodic Porous Alumina on Oriented Aluminum Grains by High Acid Concentration and High Temperature Anodization. *Nanotechnology* **2013**, *24*, 215602-1–215602-10.

47. Masuda, H.; Fukuda, K. Ordered Metal Nanohole Arrays Made by a 2-Step Replication of Honeycomb Structures of Anodic Alumina. *Science* **1995**, *268*, 1466–1468.

48. Lee, W.; Ji, R.; Gösele, U.; Nielsch, K. Fast Fabrication of Long-Range Ordered Porous Alumina Membranes by Hard Anodization. *Nat. Mater.* **2006**, *5*, 741–747.

ARTICLE

49. Cheng, C.; Xu, C.; Zhou, T.; Zhang, X. F.; Xu, Y. Temperature Dependent Complex Photonic Band Structures in Two-Dimensional Photonic Crystals Composed of High-Temperature Superconductors. *J. Phys.: Condens. Matter.* **2008**, *20*, 275203-1–275203-8.

50. Cheng, C.; Xu, C. Photonic Bands in Two-Dimensional Metallodielectric Photonic Crystals Composed of Metal Coated Cylinders. *J. Appl. Phys.* **2009**, *106*, 033101-1–033101-7.

51. Yau, S. L.; Fan, F. R. F.; Moffat, T. P.; Bard, A. J. *In Situ* Scanning Tunneling Microscopy of Ni(100) in 1 M NaOH. *J. Phys. Chem.* **1994**, *21*, 5493–5499.

52. Wu, Z.; Huang, X. L.; Wang, Z. L.; Xu, J. J.; Wang, H. G.; Zhang, X. B. Electrostatic Induced Stretch Growth of Homogeneous $\beta-Ni(OH)_2$ on Graphene with Enhanced High-Rate Cycling for Supercapacitors. *Sci. Rep.* **2014**, *4*, 3669-1–3669-8.

53. Meher, S. K.; Justin, P.; Rao, G. R. Pine-Cone Morphology and Pseudocapacitive Behavior of Nanoporous Nickel Oxide. *Electrochem. Acta* **2010**, *55*, 8388–8396.

54. Hoppe, H. W.; Strehblow, H. H. XPS and UPS Examinations of the Formation of Passive Layers on Ni in 1 M Sodium Hydroxide and 0.5 M Sulphuric Acid. *Surf. Interface Anal.* **1989**, *14*, 121–131.

55. Paik, W.; Szklarska-Smialowska, Z. Reflectance and Ellipsometric Study of Anodic Passive Films Formed on Nickel in Sodium Hydroxide Solution. *Surf. Sci.* **1980**, *96*, 401–412.

56. Hahn, F.; Beden, B.; Croissant, M. J.; Lamy, C. *In Situ* UV Visible Reflectance Spectroscopic Investigation of the Nickel Electrode-Alkaline Solution Interface. *Electrochim. Acta* **1986**, *31*, 335–342.

57. Lee, J. W.; Ahn, T.; Soundararajan, D.; Ko, J. M.; Kim, J. D. Non-Aqueous Approach to the Preparation of Reduced Graphene Oxide $\alpha-Ni(OH)_2$ Hybrid Composites and Their High Capacitance Behavior. *Chem. Commun.* **2011**, *47*, 6305–6307.

58. Sathiya, M.; Prakash, A. S.; Ramesha, K.; Tarascon, J. M.; Shukla, A. K. V_2O_5-Anchored Carbon Nanotubes for Enhanced Electrochemical Engergy Storage. *J. Am. Chem. Soc.* **2011**, *133*, 16291–16299.

59. Tu, K. N. *Electronic Thin-Film Reliability*; Cambridge University Press: Cambridge, 2011.

60. Hsueh, C. H. Modeling of Elastic Deformation of Multilayers Due to Residual Stresses and External Bending. *J. Appl. Phys.* **2002**, *91*, 9652–9656.

61. Gibson, L. J.; Ashby, M. F. *Cellular Solids: Structure and Properties*, 2nd ed.; Cambridge University Press: Cambridge, 1997.

62. Luo, J. K.; Flewitt, A. J.; Spearing, S. M.; Fleck, N. A.; Milne, W. I. Young's Modulus of Electroplated Ni Thin Film for MEMS Applications. *Mater. Lett.* **2004**, *58*, 2306–2309.

63. Fritz, T.; Griepentrog, M.; Mokwa, W.; Schnakenberg, U. Determination of Young's Modulus of Electroplated Nickel. *Electrochem. Acta* **2003**, *48*, 3029–3035.

64. Pilling, N. B.; Bedworth, R. E. The Oxidation of Metals at High Temperatures. *J. Inst. Met.* **1923**, *29*, 529–591.

65. Biener, J.; Hodge, A. M.; Hamza, A. V.; Hsiung, L. M.; Satcher, J. H. Nanoporous Au: A High Yield Strength Material. *J. Appl. Phys.* **2005**, *97*, 024301-1–024301-4.

66. Viswanath, R. N.; Kramer, D.; Weissmuller, J. Adsorbate Effects on the Surface Stress-Charge Response of Platinum Electrodes. *Electrochim. Acta* **2008**, *53*, 2757–2767.

67. Detsi, E.; Onck, P.; De Hosson, J. T. M. Metallic Muscles at Work: High Rate Actuation in Nanoporous Gold/Polyaniline Composites. *ACS Nano* **2013**, *7*, 4299–4306.

68. Hamann, C. H.; Hamnett, A.; Vielstich, W. *Electrochemistry*, 2nd ed.; Wiley-VCH: Weinheim, 2007.

69. Orazem, M. E.; Tribollet, B. *Electrochemical Impedance Spectroscopy*; Wiley: NJ, 2008.

70. Li, H. B.; Yu, M. H.; Wang, F. X.; Liang, L. Y.; Xiao, J.; Wang, C. X.; Tong, Y. X.; Yang, G. W. Amorphous Nickel Hydroxide Nanospheres with Ultrahigh Capacitance and Energy Density as Electrochemical Pseudocapacitor Materials. *Nat. Commun.* **2013**, *4*, 1894-1–1894-7.

CHENG AND NGAN

VOL. 9 ■ NO. 4 ■ 3984–3995 ■ 2015

ACSNANO

www.acsnano.org

3995